Catalysis Science & Technology

Accepted Manuscript

This article can be cited before page numbers have been issued, to do this please use: D. Vidyasagar, N. R. Manwar, A. Gupta, S. G. Ghugal, R. Boukherroub and S. S. Umare, *Catal. Sci. Technol.*, 2019, DOI: 10.1039/C8CY02220H.

ROYAL SOCIETY OF CHEMISTRY

rsc.li/catalysis

Phenyl-grafted Carbon Nitride Semiconductor for Photocatalytic CO_2 Reduction and Rapid Degradation of Organic Dyes

Devthade Vidyasagar,[a] Nilesh Manwar,[b] Akanksha Gupta,[a] Sachin G Ghugal,[c] Suresh S Umare,[a*] and Rabah Boukherroub[d]

[a] Materials and Catalysis Laboratory, Department of Chemistry, Visvesvaraya National Institute of Technology (VNIT), Nagpur, Maharashtra, 440010, India. Email: ssumare@chm.vnit.ac.in, ssumare1965@gmail.com, Fax: +91 712 2223230, Tel: +91 712 2801316.

[b] Chemical and Material Science Division (CMSD), CSIR-Indian Institute of Petroleum (IIP), Mohkampur, Dehradun, Uttarakhand, 248005, India.

[c] School of Chemistry, Univ. of Hyderabad, Telangana, 500046, India.

[d] Univ. Lille, CNRS, Centrale Lille, ISEN, Univ. Valenciennes, UMR 8520 – IEMN, F-59000 Lille, France.

Abstract: Molecular engineering of graphitic carbon nitride (g-C_3N_4) is achieved by the copolymerization of π-conjugated phenyl urea, melamine, and urea. Integration of aromatic phenyl rings into the heptazine network of g-C_3N_4 alters its structural, optical and electronic properties. The fusion of polymeric g-C_3N_4 core with aromatic phenyl groups induces band gap tuning, greatly improves the separation and lifetime of charge-carriers. As a result, CO_2 photoreduction experiments conducted by using phenyl grafted g-C_3N_4 afford methane and formic acid in high yields. Furthermore, a selective model organic pollutant rhodamine B dye is rapidly decomposed under visible light irradiation. This work suggests that pyrolysis of a suitable aromatic π-deficient molecular dopant such as phenyl urea can drastically alter the photo-response of carbon nitride photocatalyst and may enhance its photocatalytic activity. Hence, the present work is expected to be of significant value in sustainable energy production and environmental remediation.

Keywords: Carbon nitride; Phenyl grafted g-C_3N_4; CO_2 photoreduction; dye degradation; photocatalysis

Introduction

Rational design of visible active photo-systems to generate value-added chemicals from carbon dioxide (CO_2) holds great potential in solving energy calamity. Solar photocatalysis is a strategic resource to mitigate the negative effects of environment and energy crisis. So far, a wide variety of materials have been examined as visible active photocatalysts, including metal oxides,[1] metal nitrides,[2] chalcogenides,[3] phosphides,[4] metal-organic frameworks,[5] layer-double hydroxides,[6] mixed oxides,[7] hybrid composites[8] and conjugated polymers.[9] In particular, conjugated polymers are of special interest due to their low-cost, easily processable, and environmentally benign properties. Recently, two-dimensional graphitic carbon nitride (g-C_3N_4) emerged as a metal-free visible active photocatalyst.[10] Polymeric g-C_3N_4 materials are new additions to the carbon family and are highly praised as multifunctional wonder materials, rich playgrounds for solar photocatalysis.[11] Indeed, g-C_3N_4 holds enormous promise as a potential photocatalyst for environmental remediation and energy technologies.[12] The immense practical importance of g-C_3N_4 based materials is due to their unique thermal, physicochemical, optical properties (band gap of 2.7 eV), and their metal-free semiconducting

View Article Online
DOI: 10.1039/C8CY02220H

nature.[13] Although g-C_3N_4 has several exciting properties, the quantum efficiency of bulk g-C_3N_4 is still restricted by rapid charge recombination, low surface area, and limited visible light absorption.[14] This led to an upsurge in the modification of g-C_3N_4 synthetic strategies. In this context, several methods have been adopted to retard the high charge recombination rate and extend the visible light absorption of pristine g-C_3N_4.[15]

The formation of heterostructures,[16] metal-doping,[17] molecular engineering,[18] supramolecular preorganisation,[19] use of hard or soft templates,[20] and copolymerization[21] strategies have been implemented to enhance the photoactivity of bare g-C_3N_4. Direct co-polymerisation of g-C_3N_4 precursors with π-electron conjugated systems can extend the optical absorption towards longer wavelength. For instance, Zhang *et al.* exemplified that co-polymerisation of dicyandiamide with barbituric acid as the molecular dopant modified the triazine network of g-C_3N_4 and extended the optical absorption further into the visible region with superior photocatalytic properties.[22] Modification with a series of aromatic π-electron conjugated systems such as 4-amino-2,6-dihydroxypyrimidine,[23] 2,6-diaminopyridine,[24] 3-aminothiophene-2-carbonitrile,[25] 2,4-diamino-6-phenyl-1,3,5-triazine,[26] acetoguanamine,[27] thymine,[28] barbituric acid[29] and 2,4,6-triaminopyrimidine[30] was performed to significantly red shift the optical absorption edge of bulk g-C_3N_4 and improve its photoactivity. These reports recommend that incorporation of co-monomer building blocks into polymeric network of g-C_3N_4 can change the physicochemical properties and result in high photoactivity of modified g-C_3N_4.[31]

Motivated by the latest outcomes, we endeavoured to integrate phenyl urea as an aromatic π-electron conjugated motif into the g-C_3N_4 framework and inspect the impact of phenyl-grafting on photocatalytic CO_2 reduction and mineralisation of organic dyes. In this viewpoint, phenyl urea was prepared from urea and copolymerised with melamine under suitable experimental conditions.

Results and Discussion

The stepwise preparation process for phenyl grafted g-C_3N_4 is depicted in **Figure S1**. As illustrated in **Figure S2**, during thermal polymerisation the amino units of melamine and phenyl urea are involved in the polymerisation process to form phenyl grafted g-C_3N_4. The optimized molecular functionalization of g-C_3N_4 with π-electron rich phenyl urea can modulate electronic energy levels and accelerate the reaction rate. However, an excess amount of phenyl urea would deteriorate the visible light absorption, deform tri-s-triazine network and can create new recombination sites for the charge carriers. Therefore, for the optimized phenyl grafted g-C_3N_4, the amount of monomer was set to 20 mg per 10 g of urea/melamine content and the structural, morphological and electronic properties of the resulting catalyst are thoroughly investigated.

Powder X-ray diffraction (PXRD) analysis was used to ascertain the crystalline phase and structural information of as-synthesized materials. The PXRD pattern of polymeric g-C_3N_4 and Ph_{20}-g-C_3N_4 displayed unique diffraction peaks at *2θ* value of 27.50° and 27.14°, respectively, which correspond to the *hkl* (002) reflection arising from the interlayer stacking of aromatic tri-s-triazine rings **(Figure 1a)**. However, the (002)

View Article Online
DOI: 10.1039/C8CY02220H

reflection peak of Ph_{20}-g-C_3N_4 sample is comparatively broader than the peak of g-C_3N_4. This slightly wider (002) reflection of Ph_{20}-g-C_3N_4 is likely due to the incorporation of guest phenyl molecules. Compared to g-C_3N_4, the (002) reflection in the Ph_{20}-g-C_3N_4 shifted to lower diffraction angle and displayed a larger *d*-spacing value of 0.332 nm, which denotes increased interlayer distance. The addition of phenyl urea induced pronounced intensity of in-plane (100) reflection in the Ph_{20}-g-C_3N_4 sample. Furthermore, the low-intense and broad peaks of g-C_3N_4 in Ph_{20}-g-C_3N_4 suggest low-crystalline nature of the material. These crystalline rearrangements in Ph_{20}-g-C_3N_4 strongly indicate the successful integration of phenyl urea into the polymeric tri-s-triazine framework.

The optical properties of polymeric g-C_3N_4 were assessed by UV–Vis diffuse reflectance absorption spectroscopy (UV-Vis DRS). The UV-Vis spectrum of g-C_3N_4 shows an absorption band with an edge at 456 nm corresponding to the blue region, which is attributed to the intrinsic n-π* or π-π* transition of aromatic tri-s-triazine repeating units.[32] The absorbance spectrum of Ph_{20}-g-C_3N_4 exhibits a red shift of the absorption band edge from ca. 456 nm to 466 nm **(Figure 1b)**, which is likely due to π-conjugation of phenyl group as well as the excitation from band tail/localized states caused by the incomplete long-range ordering of tri-s-triazine structure.[33] It suggests that the introduction of phenyl urea alters the structural configuration of the tri-s-triazine ring and enhances the visible light harvesting capacity towards longer wavelength. Moreover, the energy band gap of g-C_3N_4 and Ph_{20}-g-C_3N_4 calculated from the Kubelka-Munk (K-M) plots were 2.72 and 2.66 eV, respectively **(Figure 1c)**. The slight red shift in energy band gap of the Ph_{20}-g-C_3N_4 is a result of additional aromatic phenyl moieties on the g-C_3N_4 network, which effectively relocate π-conjugated electrons and tailored highest occupied molecular orbital (HOMO) and lowest unoccupied molecular orbital (LUMO) energy levels.[34] The valence band (VB) and conduction band (CB) edge potential of Ph_{20}-g-C_3N_4 estimated by Mulliken electronegativity equations were +1.65 and -1.01 eV, respectively. As compared to unmodified g-C_3N_4, Ph_{20}-g-C_3N_4 showed about 0.06 eV decrease in the band gap energy, which means that phenyl grafting increased the sp^2 character in g-C_3N_4 by graphitization which leads to excess aromaticity. Further, UV-visible absorption spectrum of Ph-g-C_3N_4 displayed a broad absorption tail in the visible region, which is likely due to the n→π transition of N-C=C of newly formed aromatic phenyl ring. The estimated second optical band gap of absorption tail is found to be 1.96 eV. Thus, the Ph-g-C_3N_4 exhibits extended light absorption from UV-visible to visible region, and lower the photo-excitation energy.

Fourier transform infrared (FT-IR) analysis of synthesized materials revealed formation of graphitic carbon network. The corresponding FT-IR spectrum of Ph_{20}-g-C_3N_4 is comparable to the reported g-C_3N_4 data and shows strong stretching bands at 3200-2900 cm^{-1} (-NH/-NH_2), 1100-1576 cm^{-1} (-CN,-C=C), and 809 cm^{-1} corresponding to condensed aromatic –CN rings **(Figure 1d)**.[35] A close look in the 1600-1400 cm^{-1} region reveals a band at 1504 cm^{-1} corresponding to aromatic C=C stretch (**Figure 1e**).[36] The supramolecular assembly of phenyl urea into the tri-s-triazine framework decreased the intensity of 809 cm^{-1} signal in Ph_{20}-g-C_3N_4 sample. These characteristic alterations in graphitic carbon network are further revealed by ^{13}C solid-state cross-polarization magic angle spinning (CP-MAS) nuclear magnetic resonance (NMR) spectroscopy.

View Article Online
DOI: 10.1039/C8CY02220H

Carbon environment of g-C_3N_4 analysed by solid-state ^{13}C MAS-NMR depicts two signals at 164.6 and 156.3 ppm, which are assigned to sp^2 bonded carbon atoms of inter-linked tri-s-triazine rings and C(i)N_3 groups of the cyameluric group **(Figure 1f)**.[37] However, sp^2 carbon atoms in the Ph_{20}-g-C_3N_4 are shifted to higher values of 157.9 and 165.9 ppm (**Figure 1f**). Moreover, both signals are broadened and exhibit an increase in the resolution of the signal to noise ratio **(Figure f inset)**. This indicates the modification or disorder in the carbon environment of g-C_3N_4 network, which is ascribed to the additional effect of aromatic phenyl carbon atoms. Furthermore, indistinct broad humps in ^{13}C NMR spectrum of Ph_{20}-g-C_3N_4 at 130-140 ppm reflects C=C phenyl type environment.[38] Conversely, no clear peak of aromatic C=C was observed due to the low amount of phenyl urea in the condensation process.

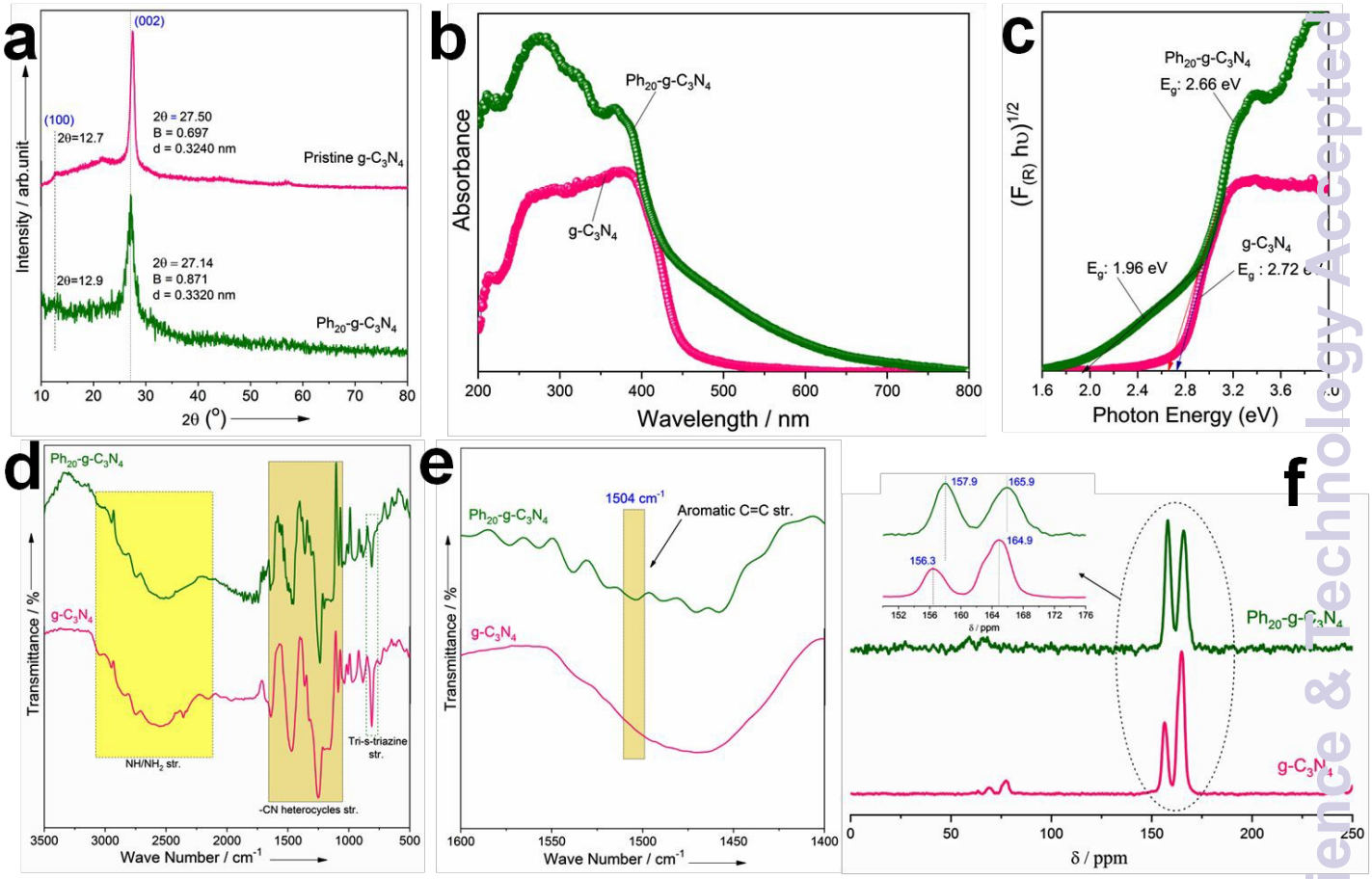

Figure 1. Characterisation details of g-C_3N_4 and Ph_{20}-g-C_3N_4: (a) powder XRD patterns, (b) UV-Vis absorbance spectra, (c) Kubelka-Munk plots, (d) FT-IR spectra, (e) enlarged portion of FT-IR spectra in the 1400-1600 cm^{-1} region, and (f) Solid state ^{13}C MAS NMR spectra.

The elemental composition and chemical states of Ph-g-C_3N_4 is characterized by X-ray photoelectron spectroscopy (XPS). The XPS survey spectra of g-C_3N_4 and Ph-g-C_3N_4 comprise two sharp peaks at ≈288.0 and 398.0 eV, which are related to the C1s and N1s elements **(Figure S3)**, respectively.[39] It is worth to note that the XPS data in **Table S1** shows an increase in carbon amount for Ph-g-C_3N_4 as compared to that of g-C_3N_4; this extra carbon contribution is likely from aromatic phenyl groups in Ph-g-C_3N_4. The high resolution C1s spectrum of g-C_3N_4 is deconvoluted into two peaks. The primary peak at binding energy of 285.2 eV is

View Article Online
DOI: 10.1039/C8CY02220H

ascribed to adventitious carbon (C-C), while the peak at 288.4 eV is originated from C-N=C coordinating units of tri-s-triazine ring.[40] The high resolution C1s XPS spectrum of Ph-g-C_3N_4 is fitted with three different carbon species. The two peaks centered at 284.8 and 288.2 eV are due to sp^2 bonded C-C atom and heterocyclic C-N=C species, respectively.[41] Notably, the sp^2 C-C bonding mode signal at 284.8 eV is profound in Ph-g-C_3N_4 C1s XPS spectrum, which corroborates the increased aromatic carbon environment in the material **(Figure S3)**. The small contribution peak found at 286.2 eV is assigned to C-O-C type linkage in Ph-g-C_3N_4.[29a] The N1s XPS spectra of g-C_3N_4 and Ph-g-C_3N_4 were nearly identical with peaks at ≈398.0, 400.0, and 404.0 eV corresponding to the contribution of C=N, N-$(C)_3$, and N-H bonding modes, respectively **(Figure S3)**.[27] Based on the XPS results, we assume that the increase in contribution of sp^2 -C=C- species can be due to the phenyl grafting of heptazine ring.

Morphological and microstructure analysis

The field emission scanning electron microscopy (FE-SEM) images of g-C_3N_4 and Ph_{20}-g-C_3N_4 displayed broken sheet-texture **(Figure 2a, d)**. Energy-dispersive X-ray spectroscopy (EDS) analysis confirmed that the materials consist mainly of carbon and nitrogen with a trace amount of oxygen contamination **(Figure 2b, e)**. The C/N molar ratio increased from 0.56 for g-C_3N_4 to 0.70 for Ph_{20}-g-C_3N_4. Besides, a slight increment in the carbon amount was observed in the Ph_{20}-g-C_3N_4 sample (**(Figure 2c, f)**). This increase in carbon content is likely due to the incorporation of aromatic phenyl urea within the g-C_3N_4 framework, which further evidences the successful engineering of g-C_3N_4 tri-s-triazine network.

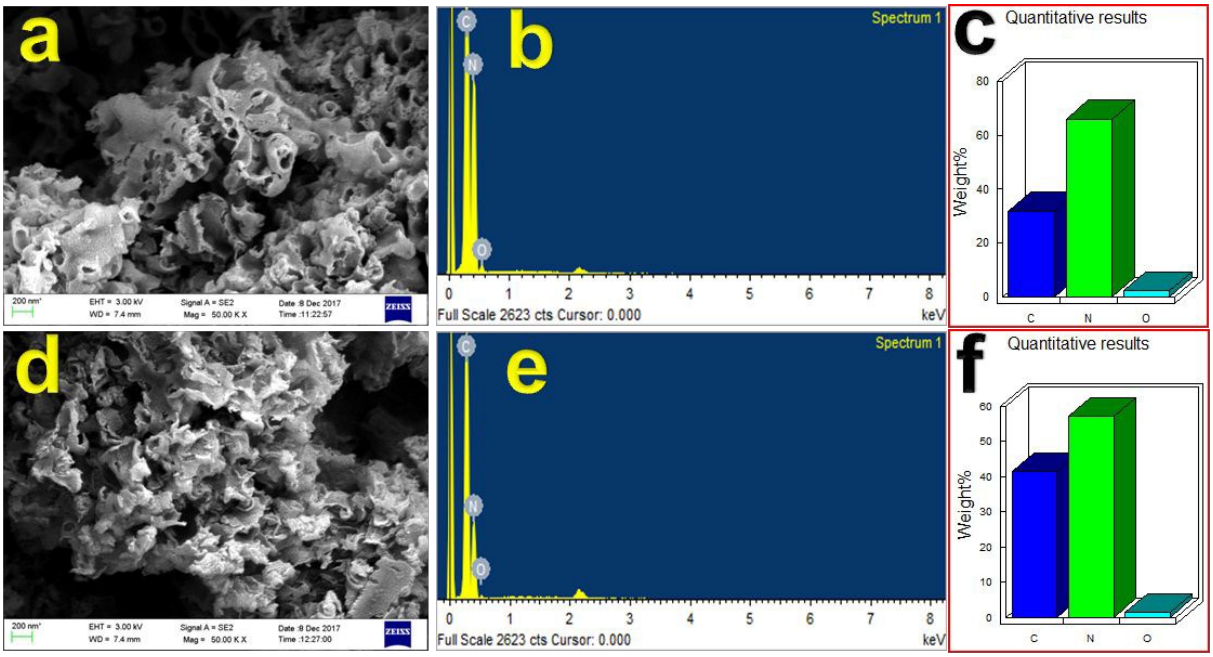

Figure 2. (a, d) FE-SEM images, (b, e) energy-dispersive X-ray spectra and quantitative elemental composition of (c) g-C_3N_4 and (f) Ph_{20}-g-C_3N_4.

The microstructure of g-C_3N_4 significantly changed with the incorporation of aromatic phenyl urea. The TEM image of g-C_3N_4 reflects transparent thin sheet structure, whereas Ph_{20}-g-C_3N_4 displays compact self-rolling appearance of g-C_3N_4 layers due to the synergistic effect of intramolecular hydrogen bonding and

View Article Online
DOI: 10.1039/C8CY02220H

van der Waals interaction **(Figure 3a, d)**. Similar TEM observations were previously obtained for melamine and 2,4,6-triaminopyrimidine copolymerised samples.[30] The integration of π-aromatic phenyl groups into tri-s-triazine network increased the 2D interplanar packing distance of heptazine units from 0.321 to 0.334 nm **(Figure 3b, e)**. The obtained interplanar (*d*-spacing plot profile, **Figure S4**) distance results are consistent with the values obtained from PXRD analysis. The selected area diffraction (SAD) pattern of g-C_3N_4 exhibits concentric rings, whereas the SAD pattern of Ph_{20}-g-C_3N_4 displays amorphous characteristics with diffuse ring pattern **(Figure 3c, f)**. These microstructural alterations in heptazine units may contribute to the enhancement of surface area and subsequently the photoactivity. The specific surface area and pore size of the developed materials were analyzed by nitrogen adsorption-desorption isotherms. The N_2 isotherms of both g-C_3N_4 and Ph_{20}-g-C_3N_4 reflected type-IV isotherms. The calculated Brunauer-Emmett-Teller (BET) specific surface area of Ph_{20}-g-C_3N_4 was determined to be 94.74 $m^2\ g^{-1}$, which was 10-fold higher than that of unmodified g-C_3N_4 (BET surface area of g-C_3N_4: 9.55 $m^2\ g^{-1}$) **(Figure S5a)**. The larger specific surface area of Ph_{20}-g-C_3N_4 could increase the area of photon incidence and expose more catalytic sites, which would be more advantageous in the photocatalytic process.

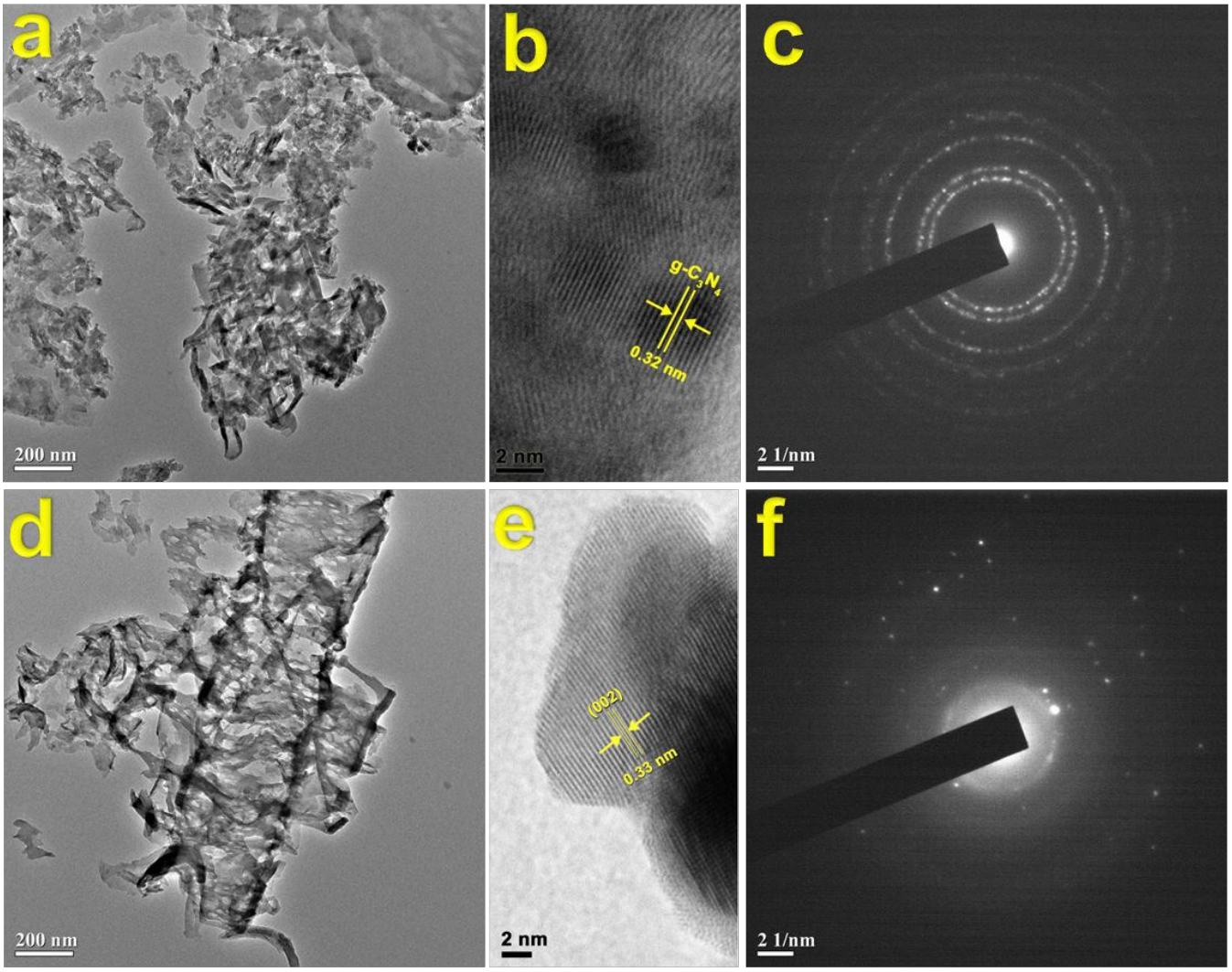

Figure 3. TEM images, HR-TEM images and SAD patterns of g-C_3N_4 (a-c) and Ph_{20}-g-C_3N_4 (d-e), respectively.

View Article Online
DOI: 10.1039/C8CY02220H

Visible light-driven CO_2 photoreduction

The CO_2 photoreduction performance of g-C_3N_4 and Ph_{20}-g-C_3N_4 catalyst was studied in a solvent mixture of *N,N*-dimethylformamide/water/triethanolamine (DMF/H_2O/TEA = 30/10/10 mL) using 100 mg of photocatalyst. After 24 h of visible light irradiation, 1 μL of sample was withdrawn and corresponding products in the reaction mixture were monitored by injecting into GC–TCD and GC–FID. All Ph_x-g-C_3N_4 samples emanated high amount of methane (CH_4) upon light irradiation. The concentration of CH_4 after 24 h of visible light irradiation using the Ph_{100}-g-C_3N_4 catalyst was 0.907 μmoles g^{-1}, which is about 4-fold higher than that produced using pure g-C_3N_4 (**Figure 4a**). The high amount of CH_4 produced by Ph_{100}-g-C_3N_4 is likely due to the availability of excess active sites on the surface with rich surface area of 78.69 m^2/g. The total amount of methanol (CH_3OH) produced was nearly 4-fold higher for Ph_{20}-g-C_3N_4 catalyst than the bulk g-C_3N_4 (**Figure 4b**) The quantum efficiency for methanol obtained from the CO_2 photoreduction system was found to be 0.96%. The details of quantum yield estimation is given in supporting information. To delight, the formic acid (HCOOH) concentration determined by HPLC analysis revealed interesting results. The HCOOH production rate after 24 h light irradiation using the Ph_{20}-g-C_3N_4 photocatalyst was 5.2 V/V% after 10-times dilution, which is significantly higher than the values reported for several photocatalysts.[42] The CO_2 photoreduction activity of metal-free Ph_{20}-g-C_3N_4 catalyst is relatively higher than or comparable to the many reported metal based photocatalysts **(Table S2)**. Furthermore, the Ph_{20}-g-C_3N_4 catalyst delivers much higher yields of methanol and formic acid, while maintaining good stability and recyclability. To circumvent the possibility of alternative carbon source in the experimental system, blank test was conducted under identical reaction conditions by replacing CO_2 with N_2 gas, which inferred no hydrocarbon products formation. This suggests that no carbon products were emanated from the photocatalyst or any other carbon contamination in the photocatalytic system.

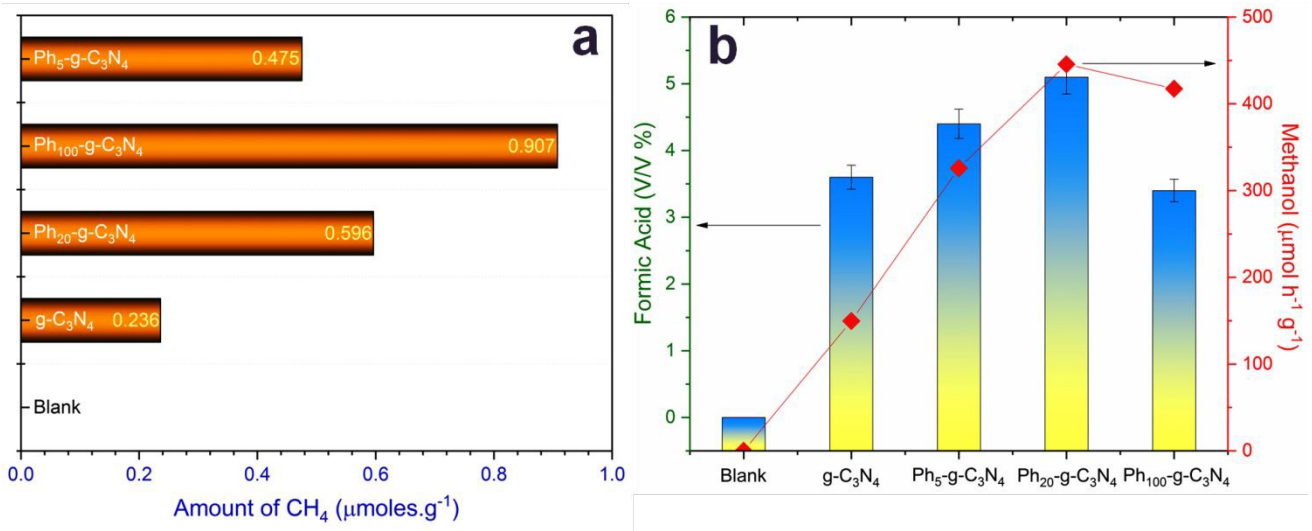

Figure 4. (a) Amount of methane formation and (b) yield of formic acid and methanol obtained in CO_2-photoreduction using g-C_3N_4 and Ph_{20}-g-C_3N_4 catalysts. Reaction conditions: 100 mg of photocatalyst; 10 mL water; 40 mL 3:1 (v/v) DMF/TEA; light source: 20W white cold LED; reaction time: 24 h.

View Article Online
DOI: 10.1039/C8CY02220H

Till date, very limited studies postulated the mechanistic aspect of CO_2 photoreduction.[43] Nevertheless, the precise acceptable CO_2 photoreduction pathway in heterogeneous catalysis is still a subject of high scrutiny. Herein, we propose a plausible reaction pathway for the formation of CH_4, CH_3OH, and HCOOH on the surface of the solid Ph_x-g-C_3N_4 catalyst. Polymeric Ph_x-g-C_3N_4 redox potentials are suitable to drive CO_2 photoreduction to hydrocarbons. At first, tri-s-triazine ring of Ph_x-g-C_3N_4 is activated by visible light irradiation, which results in the generation of electrons (e^-) in the conduction band (CB) and holes (h^+) in the valence band (VB). As illustrated in step (i) of **Figure 5**, surface adsorbed CO_2 molecules strongly interact with P_z orbitals or lone pairs of aromatic nitrogens in Ph_x-g-C_3N_4 *via* π-π stacking mode and initiate electron transfer from CB of Ph_x-g-C_3N_4 to surface-bound CO_2 forming partially charged $CO_2^{\bullet -}$ radical anion.[44] However, the complete formation of $CO_2^{\bullet -}$ radical anion is thermodynamically hindered reaction on the Ph_x-g-C_3N_4 catalyst, owing to its lower reduction potential than $CO_2/CO_2^{\bullet -}$ (-1.90 V).[45] The partial transfer of an electron to (C-O) π* orbital destabilizes the linear symmetry of CO_2 and its molecular geometry is distorted to a bent structure.[46] As a consequence, repulsions on electrophilic carbon increase, contributing to the lowering of the LUMO of bent CO_2.[47] Thus, lower potential barrier further enables multistep electron addition into the LUMO of bent CO_2. The electrons in CB of Ph_x-g-C_3N_4 have reduction potential of -1.01 eV, which is more negative than the reduction potentials of CO_2/HCOOH (-0.61 V), CO_2/CO (-0.53 V), CO_2/HCHO (-0.48 V) CO_2/CH_3OH (-0.38 V), CO_2/CH_4 (-0.24 V vs. NHE).[48] In parallel, the oxidation potential of Ph_x-g-C_3N_4 VB holes (h^+) (+1.65 eV *vs.* NHE) is sufficiently positive than the oxidation potential of H_2O/O_2 (+0.82 eV vs. NHE). As a result, multiple electrons and protons transfer may lead to the cleavage of C-O and formation of C-H bonds associated with corresponding photoreduction products (**Figure S6**).

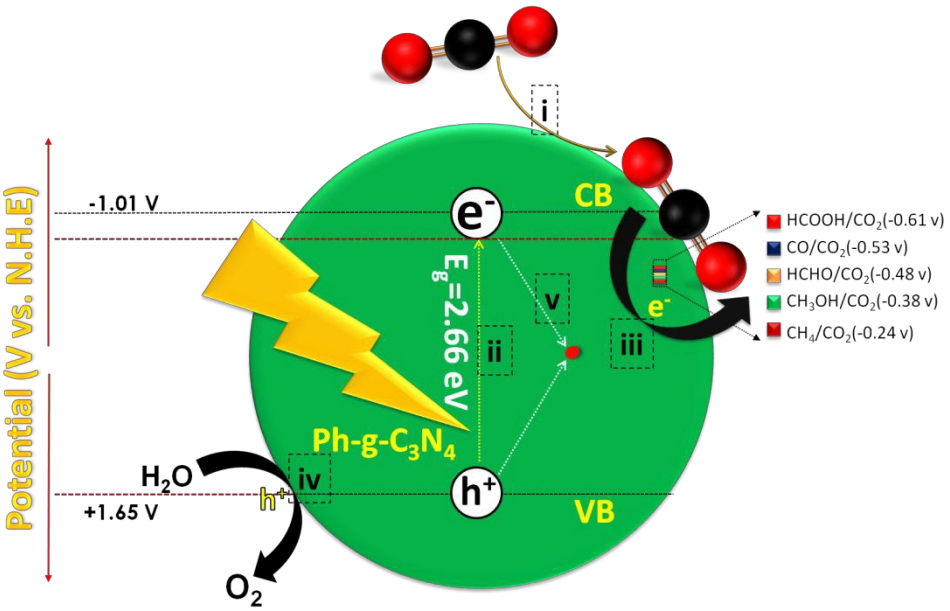

Figure 5. Schematic illustration of steps involved in CO_2 photoreduction and standard reduction potentials of corresponding CO_2 reduction products at pH 7 with reference to normal hydrogen electrode (NHE), 25°C and 1 atm gas pressure. Basic steps involved in CO_2 reduction: (i) sorption of CO_2 on the catalyst surface, (ii) photo-generation of charge carriers, (iii) photoreduction of CO_2 into suitable products, (iv) oxidation of water into O_2 and (v) recombination of electron-hole pairs.

View Article Online
DOI: 10.1039/C8CY02220H

Photocatalytic rhodamine B degradation

The improvement in photoactive performance of Ph_x-g-C_3N_4 catalysts was further assessed by investigating the degradation of RhB dye under visible-light irradiation. All phenyl grafted Ph_x-g-C_3N_4 catalysts demonstrated higher photocatalytic activity and RhB dye was fully degraded within 25 min of visible-light illumination **(Figure 6a).** Conversely**,** bulk g-C_3N4 exhibited less than 40% degradation of RhB over 30 min of light illumination. The RhB degradation can be fitted with pseudo second-order kinetics and calculated rate constant (*k*) of Ph_5-g-C_3N_4 and Ph_{100}-g-C_3N_4 are 0.252 and 0.216 min^{-1}, respectively (**Figure S7a**). Again Ph_{20}-g-C_3N_4 photocatalyst is the most efficient for RhB degradation with a rate constant (*k*) of 0.307 min^{-1}. The variation of the degradation rate of Ph_x-g-C_3N_4 samples is likely due to the difference in electronic properties among g-C_3N_4 matrix. To note, increasing the content of phenyl urea behind the optimum level may induce deformation of tri-s-triazine core and results in poor performance. Thus, higher RhB degradation activity of Ph_{20}-g-C_3N_4 sample is ascribed to the optimum content of phenyl urea. Further, the control experiment performed in the absence of photocatalyst displayed negligible degradation of RhB, suggesting that the degradation is catalytic in nature. It is well known that RhB degradation occurs *via* two pathways.[49] In first, direct cleavage of conjugated chromophore with timely decay in absorbance and the second path involves the formation of *N*-de-ethylated intermediates, which induces the blue or hypsochromic shift of characteristic absorbance maxima.[50] As shown in **Figure S7b,** the UV–visible absorption spectrum of RhB shows timely decay in absorbance at 553 nm, which corroborates the direct cleavage of C=C and C=N bonds in the conjugated chromophore.[51] It is well known that RhB degradation kinetic mainly depends on surface area of the catalyst, optical absorption and lifetime of charge carriers.[52] In the present system, integration of electron-rich phenyl urea into g-C_3N_4 framework strongly influenced the surface area and lifetime of photo-excitons, which drastically enhanced RhB degradation.

Table 1. Specific surface area, energy band gap and RhB degradation parameters.

Composition	BET surface area (m^2 g^{-1})	Energy Band Gap (eV)	RhB degradation rate constant (k), (min^{-1})
g-C_3N_4	9.55	2.72	0.038
Ph_{20}-g-C_3N_4	94.74	2.66	0.307

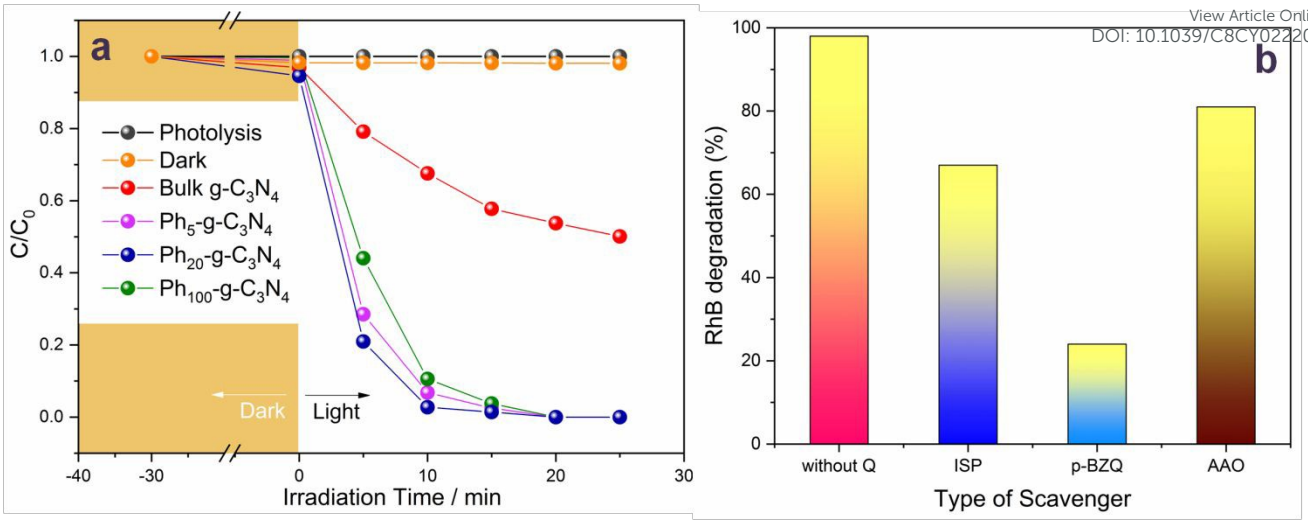

Figure 6. (a) Change in relative concentration of RhB as a function of irradiation time and (b) Effect of charge-carrier quenchers on RhB degradation over Ph_{20}-g-C_3N_4 catalyst. The bars indicate percentage of RhB dye degradation after 25 min light irradiation.

To identify the role of reactive oxidative species (ROS) involved in rapid photodegradation of RhB, charge-trapping experiments were performed. Use of *p*-benzoquinone as a scavenger effectively suppressed the RhB degradation rate, implying superoxide radical anion ($O_2^{\bullet -}$) is the main ROS in the system and plays a major role in fast mineralization of RhB. Although, other scavengers showed moderate effect on the rate of RhB degradation, the $O_2^{\bullet -}$ quenching was pronounced **(Figure 6b)**. Under visible light irradiation, photo-induced electron transfer from CB of Ph-g-C_3N_4 to the dissolved oxygen results in the formation $O_2^{\bullet -}$.[53] This reaction is thermodynamically feasible in the present system due to the fact that the CB of Ph-g-C_3N_4 (CB: -1.01 eV *vs.* NHE) is more negative than the standard reduction potential of $O_2/O_2^{\bullet -}$ (-0.046 *vs.* NHE).[54] In contrast, the VB (+1.65 V *vs.* NHE) reduction potential of Ph-g-C_3N_4 is lower than the reduction potential of $OH^-/OH^\bullet$ (+2.7 V *vs.* NHE), and thus cannot produce $OH^\bullet$ upon reaction of H_2O with VB holes.[55] Based on the scavenger experiments, the possible repetitive reactions occurring on the surface of catalyst are proposed. The formation of these highly active ROS resulted in the rapid decomposition of RhB. Henceforth, the effective species responsible for RhB degradation was $O_2^{\bullet -}$, $OH^\bullet$ and holes have a minor effect on the degradation rate.[56] Alternatively, a possible photosensitized electron transfer mechanism occurring on the surface of Ph_{20}-g-C_3N_4 catalyst is likely to occur (**Figure 7**).

$$Ph\text{-}g\text{-}C_3N_4 + h\nu \rightarrow e^-_{[CB]} + h^+_{[VB]} \quad \text{(i)}$$

$$O_2 + e^-_{[CB]} \rightarrow O_2^{\bullet -} \quad -0.2\ V \quad \text{(ii)}$$

$$O_2^{\bullet -} + 2H_2O + 2e^-_{[CB]} \rightarrow 3OH^- + OH^\bullet \quad +0.2\ V \quad \text{(iii)}$$

$$OH^- + h^+_{[VB]} \rightarrow OH^\bullet \quad +1.3\ V \quad \text{(iv)}$$

$$OH^\bullet + RhB \rightarrow CO_2 + H_2O \quad \text{(v)}$$

$$h^+_{[VB]} + RhB \rightarrow CO_2 + H_2O \quad \text{(vi)}$$

View Article Online
DOI: 10.1039/C8CY02220H

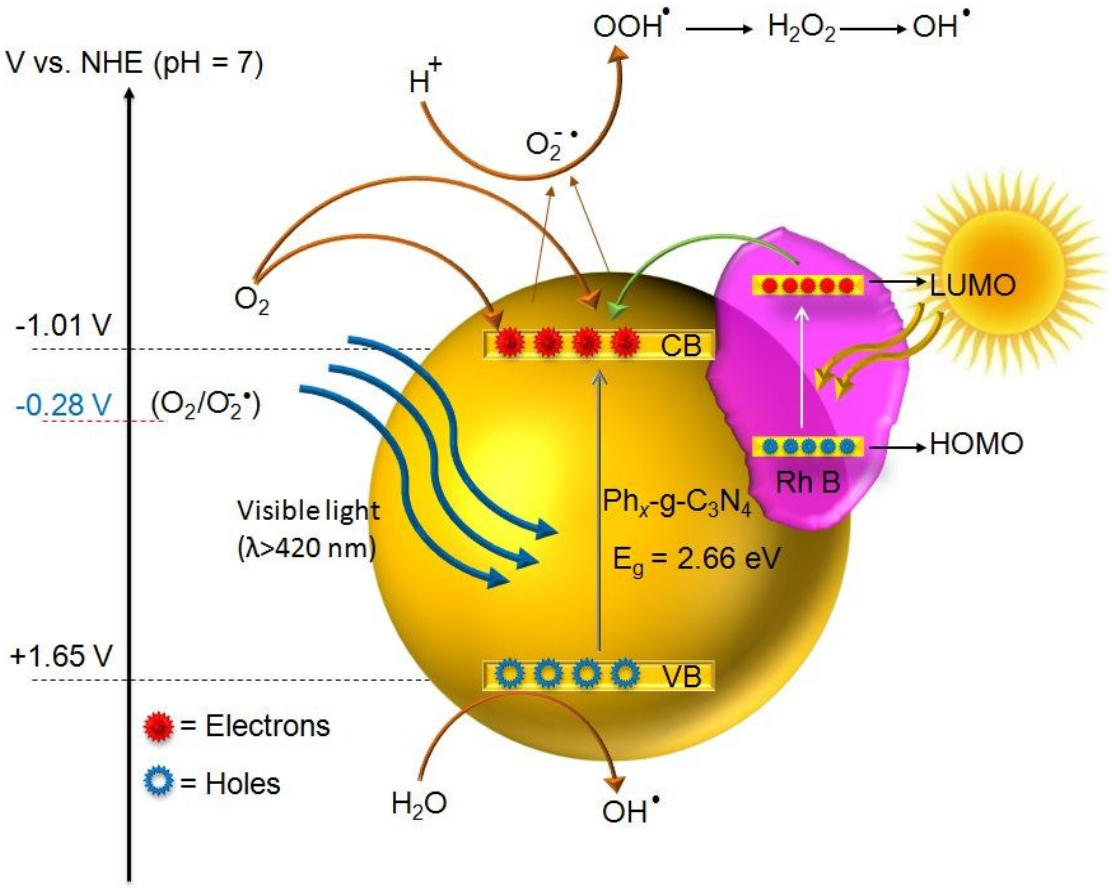

Figure 7. The schematic mechanism of photosensitized electron injection and formation of hydroxyl radicals by the excitation of Ph-g-C_3N_4 under visible light irradiation**.**

Recyclability test of catalyst

Recyclability study unravels the stability of catalyst for practical application. Repetitive RhB photodegradation experiments were performed using the same recycled catalyst. After each cycle, the photocatalyst was separated by centrifugation and repeatedly washed with deionized water, acetone and dried in air oven for 24 h. Interestingly, Ph_{20}-g-C_3N_4 catalyst was robust and retained high photoactivity for four cycles **(Figure S8a)**. The robustness of catalyst was also assessed by cyclic CO_2 reduction experiments using the same catalyst under identical conditions. As shown in **Figure S8b**, the methanol generation after five cycles was almost the same as of fresh catalyst. Furthermore, FT-IR analysis of the samples recorded after each cycle shows strong bonding modes of tri-s-triazine ring **(Figure S8c)**, suggesting high structural stability of catalyst for long-term practical applications. To determine the structural changes in Ph-g-C_3N_4 catalyst after five cycles, PXRD and SEM image of recycled catalyst were recorded (**Figure S8d, e**), which demonstrated characteristic features of pristine g-C_3N_4 and 2D morphology of catalyst. These results reflect that the developed catalyst is highly stable and efficient towards CO_2 to methanol photoconversion. The zeta potential of g-C_3N_4 dispersed in Milli-Q water was -21.4 mV whereas that of Ph-g-C_3N_4 was -11.2 mV. The higher zeta potential value of Ph-g-C_3N_4 further indicates its colloidal stability in the water medium at pH 7. In parallel, the

View Article Online
DOI: 10.1039/C8CY02220H

water dispersion study of Ph_{20}-g-C_3N_4 shows high colloidal stability for five days **(Figure S9)**, suggesting the easy access to active catalytic sites to promote the photoactivity.

Mechanistic aspects of photoactivity enhancement

To unravel the charge-dynamic kinetics of photo-excitons, room temperature photoluminescence (PL) analysis was performed at an excitation wavelength of λ=360 nm. The PL spectrum of g-C_3N_4 displayed a peak at 470 nm, which is due to band-to-band recombination of charge-carriers. The emission spectrum of Ph_{20}-g-C_3N_4 exhibited a blue–shifted peak at 460 nm, which indicates an up-shifting of the conduction band caused by the depletion of charge carriers.[57] The wider energy band gap of the g-C_3N_4 was further confirmed by the red-shift of the fluorescence emission spectrum by 10 nm due to quantum size effect. Further, PL quenching suggests that recombination of radiative electron-hole pair in Ph_{20}-g-C_3N_4 was greatly suppressed due to the extra planar π-aromatic rings **(Figure 8a)**. The charge carrier lifetimes of g-C_3N_4 and Ph_{20}-g-C_3N_4 were measured by time-resolved PL (TRPL) *via* time-correlated single photon counting (TCSPC) at the wavelength of the maximum emission peak. In the TRPL spectra, Ph_{20}-g-C_3N_4 showed slower decay kinetics compared to g-C_3N_4, which may be attributed to the improved electron transport and/or change in electronic band structure induced by the π-conjugated phenyl groups **(Figure 8b)**. The average carrier lifetime of the bulk g-C_3N_4 and Ph_{20}-g-C_3N_4 were 1.51 ns and 2.20 ns, respectively. The improvement in average lifetime of charge carriers in the Ph_{20}-g-C_3N_4 is due to the retarded recombination rate which indicates that extended band tail is involved in electron-hole recombination of Ph_{20}-g-C_3N_4. The band tails can act as electronic trapping states of electron-hole pair and consequently increase the lifetime.[58] The fluorescence lifetime imaging microscopy (FLIM) produced distinctive contrast images corresponding to the exponential decay rate of fluorescence lifetime in g-C_3N_4 and Ph_{20}-g-C_3N_4 samples **(Figure 8i-ii)**. Here, the fluorescence lifetime is the time taken by the fluorophore to remain in the excited state before returning back to the ground state.[59] The FLIM creates contrast images based on the fluorescence lifetime of an individual component and the average lifetime is colour coded. The high contribution from long lived fluorophore components of the Ph_{20}-g-C_3N_4 is detected in the green region. The green FL distribution can be clearly distinguished in both g-C_3N_4 and Ph_{20}-g-C_3N_4 FLIM images.

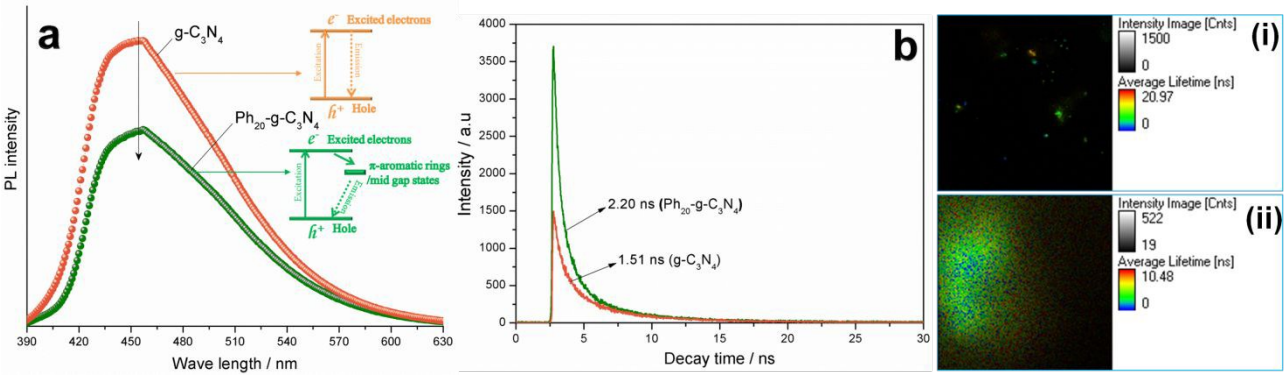

Figure 8. (a) Photoluminescence (PL) emission spectra and (b) Time-resolved PL lifetime decay spectra of g-C_3N_4 and Ph_{20}-g-C_3N_4. PL-decay plot is obtained with the excitation wavelength of 405 nm from a picosecond pulsed diode laser at room temperature and corresponding FLIM images of (i) g-C_3N_4 and (ii) Ph_{20}-g-C_3N_4.

View Article Online
DOI: 10.1039/C8CY02220H

Conclusions

We emphasize that suitable electron rich π-organic moiety such as phenyl group can significantly alter the physicochemical properties of g-C_3N_4 and can enhance its photocatalytic property. The photocatalytic activity of Ph-g-C_3N_4 samples towards CO_2 reduction and RhB degradation was significantly enhanced compared to unmodified g-C_3N_4 photocatalyst. The copolymerisation of amino/cyano precursors with nucleophile containing aromatic compounds facilitates incorporation of electron deficient π-extended aromatic groups into the g-C_3N_4 network. The bottom-up strategy of molecular doping offers the tuning of g-C_3N_4 electronic properties, increases the lifetime of charge carriers and promotes photoactivity. However, the amount of molecular dopant is extremely critical to maintain the tri-s-triazine core structure; excess content of molecular dopant can collapse the g-C_3N_4 network, resulting in poor photoactivity. In this regard, identifying relevant functional groups to extend optical absorption property of g-C_3N_4 can pave new directions in metal-free semiconductor photocatalysis. Further, high temperature of pyrolysis is a great challenge to preserve the π-conjugation of molecular dopant. Therefore, research developments on π-extended g-C_3N_4 materials have long scope and thus the present study can be of vital interest. We believe that in near future modified π-extended g-C_3N_4 photocatalysts can find potential applications in solar cells and water-splitting electrodes.

Experimental Section

Synthesis of Phenyl-Urea

Phenyl urea is synthesized by adopting previously reported procedure with certain laboratory modification.[60] In detail, about 20 g of urea and 12 g of aniline were dissolved in 100 mL of deionized water and transferred into 250 mL of round bottom flask fitted with reflux condenser. To this reaction mixture about 5 mL of HCl (4 M) and 2 mL glacial acetic acid were instantly added and the resulting mixture was refluxed at 140°C for 2 h. Then, the warm flask containing undissolved precipitate of diphenyl urea and hot liquid phase phenyl urea were separated by filtration. Finally, the hot phenyl urea solution was thoroughly crystallized in ice-cold bath.

Synthesis of Phenyl grafted g-C_3N_4

A mixture of urea (10 g) and phenyl urea (10, 20, 50, 100 and 200 mg) were ground together for at least 30 min using mortar pestle and transferred into silica crucible. The corresponding mixture was covered with a thin layer of melamine (1.5 g), capped and calcined in air furnace at 550°C for 2h. A schematic stepwise synthetic procedure is given in **Figure S2**. The advantage of thin layer of melamine is to prevent the rapid evaporation of contents and improve the reaction yield. Indeed, condensation performed without melamine protection gave no product. A plausible mechanism for the formation of Ph_{20}-g-C_3N_4 network is illustrated in **Figure S3**. The final solid samples were grounded into fine powders and denoted as Ph_x-g-C_3N_4, where '*x*' corresponds to the amount of phenyl-urea content in milligrams. For comparison, pure g-C_3N_4 was synthesized by a direct polymerisation of melamine under similar calcination temperature.

Acknowledgments

View Article Online
DOI: 10.1039/C8CY02220H

D. Vidyasagar acknowledges director VNIT, Nagpur for a research fellowship. NM likes to acknowledge HRDG-CSIR, New Delhi for the award of CSIR-Nehru Science Postdoctoral Research Fellow with their fiscal assistance. Sachin G. Ghugal would like to thank DST-SERB National Postdoctoral Fellowship scheme, Govt. of India for research funding (PDF/2017/002951). SSU is thankful to DST-SERB for financial assistance through project number SB/EMEQ-052/2014SERB. Authors also thank IISc, Bangalore NMR Facility, SAIF-IIT Madras, SAIF-Shillong, and SAIF-Chandigarh for characterization support.

References

[1] A. Fujishima, K. Honda, *Nature* **1972**, *238*, 37-38.
[2] K. Maeda, T. Takata, M. Hara, N. Saito, Y. Inoue, H. Kobayashi, K. Domen, *J. Am. Chem. Soc.* **2005**, *127*, 8286-8287.
[3] E. Lhuillier, S. Pedetti, S. Ithurria, B. Nadal, H. Heuclin, B. Dubertret, *Acc. Chem. Res.* **2015**, *48*, 22-30.
[4] a) M. Sharon, G. Tamizhmani, *J. Mater; Sci.* **1986**, *21*, 2193-2201; b) G. Liao, N. Luo, K.-Q. Chen, H. Xu, *Sci. Rep.* **2016**, *6*, 28240; c) W. E. Buhro, *Polyhedron* **1994**, *13*, 1131-1148.
[5] M. Usman, S. Mendiratta, K. L. Lu, *Adv. Mater.* **2017**, *29*.
[6] L. Mohapatra, K. Parida, *J. Mater. Chem. A* **2016**, *4*, 10744-10766.
[7] Z. Zou, H. Arakawa, *J. Photochem. Photobiol. A* **2003**, *158*, 145-162.
[8] M. Tamborra, M. Striccoli, R. Comparelli, M. Curri, A. Petrella, A. Agostiano, *Nanotechnology* **2004**, *15*, S240.
[9] H. Sirringhaus, P. Brown, R. Friend, M. M. Nielsen, K. Bechgaard, B. Langeveld-Voss, A. Spiering, R. A. Janssen, E. Meijer, P. Herwig, *Nature* **1999**, *401*, 685-688.
[10] X. Wang, K. Maeda, A. Thomas, K. Takanabe, G. Xin, J. M. Carlsson, K. Domen, M. Antonietti, *Nat. Mater.* **2009**, *8*, 76-80.
[11] J. C. Bian, C. Huang, R. Q. Zhang, *ChemSusChem* **2016**, *9*, 2723-2735.
[12] a) G. Algara-Siller, N. Severin, S. Y. Chong, T. Bjorkman, R. G. Palgrave, A. Laybourn, M. Antonietti, Y. Z. Khimyak, A. V. Krasheninnikov, J. P. Rabe, U. Kaiser, A. I. Cooper, A. Thomas, M. J. Bojdys, *Angew. Chem., Int. Ed.* **2014**, *53*, 7450-7455; bD. Vidyasagar, K. Gopichand, G. S. G, C. K. H., U. S. S, *ChemistrySelect* **2018**, *3*, 4009-4014.
[13] J. J. Zhu, P. Xiao, H. L. Li, S. A. C. Carabineiro, *ACS Appl. Mater. Interfaces* **2014**, *6*, 16449-16465.
[14] J. Liu, H. Q. Wang, M. Antonietti, *Chem. Soc. Rev.* **2016**, *45*, 2308-2326.
[15] S. W. Cao, J. X. Low, J. G. Yu, M. Jaroniec, *Adv. Mater.* **2015**, *27*, 2150-2176.
[16] a) S. Cao, J. Yu, *J. Phys. Chem. Lett.* **2014**, *5*, 2101-2107; b) D. Vidyasagar, S. G. Ghugal, A. Kulkarni, P. Mishra, A. G. Shende, Jagannath, S. S. Umare, R. Sasikala, *Appl. Catal. B* **2018**, *221*, 339-348; c) V. Devthade, A. Gupta, S. S. Umare, *ACS Appl. Nano Mater.* **2018**.
[17] a) Y. G. Wang, Y. G. Li, X. Bai, Q. Cai, C. L. Liu, Y. H. Zuo, S. F. Kang, L. F. Cui, *Catal. Commun.* **2016**, *84*, 179-182; b) X. Wang, X. Chen, A. Thomas, X. Fu, M. Antonietti, *Adv. Mater.* **2009**, *21*, 1609-1612.
[18] Z. Zhou, Y. Zhang, Y. Shen, S. Liu, Y. Zhang, *Chem. Soc. Rev.* **2018**, *47*, 2298-2321.
[19] J. Barrio, M. Shalom, *ChemCatChem* **2018**.
[20] Z. Yang, Y. Zhang, Z. Schnepp, *J. Mater. Chem. A* **2015**, *3*, 14081-14092.
[21] W. Ho, Z. Zhang, W. Lin, S. Huang, X. Zhang, X. Wang, Y. Huang, *ACS Appl. Mater. Interfaces* **2015**, *7*, 5497-5505.
[22] J. Zhang, X. Chen , K. Takanabe, K. Maeda, K. Domen, J. D. Epping, X. Fu, M. Antonietti, X. Wang, *Angew. Chem., Int. Ed.* **2010**, *49*, 441-444.
[23] M. Zhang, X. Wang, *Energy Environ. Sci.* **2014**, *7*, 1902-1906.
[24] Z. Chen, P. Sun, B. Fan, Q. Liu, Z. Zhang, X. Fang, *Appl. Catal. B* **2015**, *170-171*, 10-16.
[25] J. Zhang, M. Zhang, S. Lin, X. Fu, X. Wang, *J. Catal.* **2014**, *310*, 24-30.
[26] Y. Ishida, L. Chabanne, M. Antonietti, M. Shalom, *Langmuir* **2014**, *30*, 447-451.
[27] S. Wan, M. Ou, Q. Zhong, S. Zhang, W. Cai, *Adv. Opt. Mater.* **2017**, *5*, 1700536.
[28] S. Wan, Q. Zhong, M. Ou, S. Zhang, *RSC Adv.* **2016**, *6*, 101208-101215.
[29] a) J. Barrio, L. Lin, X. Wang, M. Shalom, *ACS Sustain. Chem. Eng.* **2018**, *6*, 519-530; b) Q. Zheng, D. P. Durkin, J. E. Elenewski, Y. Sun, N. A. Banek, L. Hua, H. Chen, M. J. Wagner, W. Zhang, D. Shuai, *Environ. Sci. Technol.* **2016**, *50*, 12938-12948.
[30] W. Ho, Z. Zhang, W. Lin, S. Huang, X. Zhang, X. Wang, Y. Huang, *ACS Appl. Mater. Interfaces* **2015**, *7*, 5497-5505.

[31] J. Zhang, G. Zhang, X. Chen, S. Lin, L. Möhlmann, G. Dołęga, G. Lipner, M. Antonietti, S. Blechert, X. Wang, *Angew. Chem., Int. Ed.* **2012**, *124*, 3237-3241.
[32] M. Deifallah, P. F. McMillan, F. Corà, *J. Phys. Chem., C* **2008**, *112*, 5447-5453.
[33] Y. Kang, Y. Yang, L. C. Yin, X. Kang, L. Wang, G. Liu, H. M. Cheng, *Adv. Mater.* **2016**, *28*, 6471-6477.
[34] H. Yao, L. Ye, H. Zhang, S. Li, S. Zhang, J. Hou, *Chem. Rev.,* **2016**, *116*, 7397-7457.
[35] X. Yuan, K. Luo, K. Zhang, J. He, Y. Zhao, D. Yu, *J. Phy. Chem., A* **2016**, *120*, 7427-7433.
[36] W.-D. Zhang, M. Sun, K. Li, Y.-X. Yu, *Chem. – Asian J.*, DOI: 10.1002/asia.201801083.
[37] B. Jürgens, E. Irran, J. Senker, P. Kroll, H. Müller, W. Schnick, *J. Am. Chem. Soc.* **2003**, *125*, 10288-10300.
[38] Z. Song, Z. Li, L. Lin, Y. Zhang, T. Lin, L. Chen, Z. Cai, S. Lin, L. Guo, F. Fu, *Nanoscale* **2017**, *9*, 17737-17742.
[39] J. Fu, B. Zhu, C. Jiang, B. Cheng, W. You, J. Yu, *Small* **2017**, *13*, 1603938.
[40] J. Sun, R. Phatake, A. Azoulay, G. Peng, C. Han, J. Barrio, J. Xu, X. Wang, M. Shalom, *Chemistry – A European J.,* **2018**, *24*, 14921-14927.
[41] Z. Chen, A. Savateev, S. Pronkin, V. Papaefthimiou, C. Wolff, M. G. Willinger, E. Willinger, D. Neher, M. Antonietti, D. Dontsova, *Adv. Mater.* **2017**, *29*, 1700555.
[42] (a) Y. He, Y. Wang, L. Zhang, B. Teng, M. Fan, *Appl. Catal., B* **2015**, *168*, 1-8; (b) S.-W. Cao, X.-F. Liu, Y.-P. Yuan, Z.-Y. Zhang, Y.-S. Liao, J. Fang, S. C. J. Loo, T. C. Sum, C. Xue, *Appl. Catal., B* **2014**, *147*, 940-946; (c) W.-J. Ong, L. K. Putri, L.-L. Tan, S.-P. Chai, S.-T. Yong, *Appl. Catal., B* **2016**, *180*, 530-543; (d) F. Raziq, Y. Qu, M. Humayun, A. Zada, H. Yu, L. Jing, *Appl. Catal., B* **2017**, *201*, 486-494; (e) Y. He, L. Zhang, B. Teng, M. Fan, *Environ. Sci. Technol.* **2014**, *49*, 649-656; (f) P. Niu, Y. Yang, C. Y. Jimmy, G. Liu, H.-M. Cheng, *Chem. Commun.* **2014**, *50*, 10837-10840; (g) H. Shi, G. Chen, C. Zhang, Z. Zou, *ACS Catal.* **2014**, *4*, 3637-3643.
[43] (a) K. Mori, H. Yamashita, M. Anpo, *RSC Adv.* **2012**, *2*, 3165-3172; (b) I. A. Shkrob, T. W. Marin, H. He, P. Zapol, *J. Phys. Chem., C* **2012**, *116*, 9450-9460; (c) G. Yin, M. Nishikawa, Y. Nosaka, N. Srinivasan, D. Atarashi, E. Sakai, M. Miyauchi, *ACS Nano* **2015**, *9*, 2111-2119.
[44] X. Chang, T. Wang, J. Gong, *Energ. Environ. Sci.* **2016**, *9*, 2177-2196.
[45] Y. Ji, Y. Luo, *ACS Catal.* **2016**, *6*, 2018-2025.
[46] C.-C. Yang, Y.-H. Yu, B. van der Linden, J. C. S. Wu, G. Mul, *J. Am. Chem. Soc.* **2010**, *132*, 8398-8406.
[47] V. P. Indrakanti, J. D. Kubicki, H. H. Schobert, *Energ. Environ. Sci.* **2009**, *2*, 745-758.
[48] H. S. N., S. M. Lukas, S. J. K., *Angew. Chem., Int. Ed.* **2013**, *52*, 7372-7408.
[49] M. Yin, Z. Li, J. Kou, Z. Zou, *Environ. Sci. Technol.* **2009**, *43*, 8361-8366.
[50] Y. Fan, G. Chen, D. Li, Y. Luo, N. Lock, A. P. Jensen, A. Mamakhel, J. Mi, S. B. Iversen, Q. Meng, *Int. J. Photoenergy* **2012**, *2012*.
[51] H. Fu, C. Pan, W. Yao, Y. Zhu, *J. Phys. Chem., B* **2005**, *109*, 22432-22439.
[52] S. G. Kumar, L. G. Devi, *J. Phys. Chem., A* **2011**, *115*, 13211-13241.
[53] Y. Hong, Y. Jiang, C. Li, W. Fan, X. Yan, M. Yan, W. Shi, *Appl. Catal., B* **2016**, *180*, 663-673.
[54] Z. Peng, Y. Jiaguo, J. Mietek, *Adv. Mater.* **2014**, *26*, 4920-4935.
[55] S. Kumar, A. Baruah, S. Tonda, B. Kumar, V. Shanker, B. Sreedhar, *Nanoscale* **2014**, *6*, 4830-4842.
[56] X. Liu, N. Chen, Y. Li, D. Deng, X. Xing, Y. Wang, *Sci. Rep.* **2016**, *6*, 39531.
[57] Q. Liang, Z. Li, X. Yu, Z. H. Huang, F. Kang, Q. H. Yang, *Adv. Mater.* **2015**, *27*, 4634-4639.
[58] H.-Q. Xu, J. Hu, D. Wang, Z. Li, Q. Zhang, Y. Luo, S.-H. Yu, H.-L. Jiang, *J. Am. Chem. Soc.* **2015**, *137*, 13440-13443.
[59] L.-C. Chen, W. R. Lloyd, C.-W. Chang, D. Sud, M.-A. Mycek, in *Methods in Cell Biology, Vol. 114* (Eds.: G. Sluder, D. E. Wolf), Academic Press, **2013**, pp. 457-488.
[60] S. Verma, R. Hashim, N. Krishnarth, *Indo. Global J. Pharm. Sci.* **2013**, *3*, 33-39.